

Image-Based Metrics in Ultrasound for Estimation of Global Speed-of-Sound

Roman Denkin and Orcun Goksel

Department of Information Technology, Uppsala University, Sweden

Abstract—Accurate speed-of-sound (SoS) estimation is crucial for ultrasound image formation, yet conventional systems often rely on an assumed value for imaging. While several methods exist for SoS estimation, they typically depend on complex physical models of acoustic propagation. We propose to leverage conventional image analysis techniques and metrics, as a novel and simple approach to estimate tissue SoS. We study eleven metrics in three categories for assessing image quality, image similarity and multi-frame variation, by testing them in numerical simulations and phantom experiments. Among single-frame image quality metrics, conventional Focus and our proposed Smoothed Threshold Tenengrad metrics achieved satisfactory accuracy, however only when applied to compounded images. Image quality metrics were largely surpassed by various image comparison metrics, which exhibited errors consistently under 8 m/s even applied to a single pair of images. Particularly, Mean Square Error is a computationally efficient alternative for global estimation. Mutual Information and Correlation are found to be robust to processing small image segments, making them suitable, e.g., for multi-layer SoS estimation. The above metrics do not require access to raw channel data as they can operate on post-beamformed data, and in the case of image quality metrics they can operate on B-mode images, given that the beamforming SoS can be controlled for beamforming using a multitude of values. These image analysis based SoS estimation methods offer a computationally efficient and data-accessible alternative to conventional physics-based methods, with potential extensions to layered or local SoS imaging.

Index Terms—Beamforming, biomarkers, image quality, ultrasonic imaging, ultrasound

I. INTRODUCTION

Ultrasound imaging systems collect time-domain data that requires projection into the spatial domain to create images of internal tissue structures. This process, known as beamforming, forms the foundation for many ultrasound-based downstream imaging techniques. The conversion between the domains of time and space necessitates knowledge of the conversion factor, specifically the speed-of-sound (SoS) in the imaged sample. Typically an assumed region-specific SoS (e.g., 1540 m/s) is used. However, the actual SoS values can vary significantly across the population and between different tissue types [1]. The oversimplification to an assumed constant value leads to various imaging artifacts, such as localization and smoothing artifacts with reduced image resolution. To address these limitations, multiple methods have been developed to estimate tissue SoS based on various physical models of sound propagation. Second-order polynomials are fitted to echo profiles in [2]. Speckle shifts between frames obtained from multiple different transmit events were minimized in [3].

Multiple methods employ optimization of some quantity calculated from images beamformed using different assumed SoS values. A focus quality metric based on frequency spectrum analysis is maximized in [4]. In [5], a correlation-based metric is maximized, which measures restoration quality of deconvolutions of RF ultrasound data with point-spread functions (PSFs) simulated at different sound speeds. Minimum average phase variance optimization of RF channel data after applying the dynamic focusing delay patterns is used in [6]. The above method was extended in [7] with the optimization of minimum average sum of the absolute difference of raw radio-frequency (RF) data during receive beamforming. Ultrasound speckle shape, quantified by full-width-at-half-maximum of autocovariance function, is maximized in [8]. In [9], coherence factor is maximized to search for mean SoS. Signal coherence between different transmit (Tx) and receive (Rx) paths was optimized in plane-wave imaging in [10]. In [11], a phase-based quality metric that analyzes phase uniformity along hyperbolic signal paths during delay-and-sum beamforming is maximized.

Several methods above use the term *mean* (medium) SoS when referring to the optimal homogeneous-equivalent single SoS value for an imaged region. Note that this can be somewhat misleading since the mean (average) value of a heterogeneous SoS distribution would not optimize the image appearance, but instead the SoS value that statistically optimizes the beamforming time-delays need be found to optimize the average image quality within a region [3]. Conversely, any method that optimizes the image quality in a region would find such *global* SoS value. Accordingly, when referring to a homogeneous-equivalent SoS value for a region, we prefer the term *global* instead. Several downstream US processing tasks also rely on such beamforming SoS setting. For instance, shear-wave elastography measurements were shown to potentially vary largely with SoS variation in [12]. Additionally, local tissue SoS reconstruction method also often rely on the accuracy of the initial global SoS assumption [3].

In this study, we propose a novel approach that leverages image-analysis techniques widely used in photography and other imaging applications, e.g., for adjusting focusing, to assess image quality and to quantify similarity of ultrasound images beamformed with varying SoS values. These image processing techniques may provide a robust alternative for determining accurate SoS values, both for signal-to-image conversion as well as diagnostic biomarker in ultrasound imaging. By studying image processing methods, we aim to develop an SoS estimation approach that reduces reliance on physics-based models, which may depend on sequence choices and machine specifics, be lengthy to compute, complex to

formalize, and hence potentially containing approximations and inaccuracies in their formulation. A purely image-based approach could thus be more generalizable and wider applicable, also thanks to the easier access to beamformed processed data.

II. METHODS

We study multiple image analysis metrics in three distinct categories:

- A. *Image quality* metrics evaluate focusing-related image features and can be computed on a single image frame (while they can also be applied on compounded frames for increased signal-to-noise ratio). These methods utilize the assumption and hypothesis that the images should be maximally-focused (least-blurred) when the beamforming SoS is set equivalent to the tissue value.
- B. *Image similarity* metrics compare two frames covering the same imaging area but obtained with different Tx events. This utilizes the fact that the image pixels with different Tx paths would shift with respect to each other (either constantly across the image or a function of location, given the sequence), which will co-align at the correct setting of beamforming SoS.
- C. *Multi-frame statistic* metrics that analyze pixel intensity distributions between multiple (many) frames covering the same imaging area, as an extension of the frame-pair alignment assumption above to multi-frame statistics.

To determine the optimal tissue SoS, we evaluate these metrics across a range of SoS values and define the ideal SoS value that optimizes the metric. Although various optimization methods could be employed for such search, as we aim to assess metrics optimality agnostic to optimization approaches, in this work we compute metric values on a fine resolution across a predefined range of SoS settings, which corresponds to grid-search optimization. Based on the optimality characteristics of individual metrics, in practical settings one can implement them on coarser evaluation grids, by interpolations in-between, and/or using iterative approaches over incoming frames.

Our processing pipeline for finding the optimal SoS employs the RF ultrasound echo data $\{R_1, \dots, R_{n_t}\}$ from n_t Tx events, where n_t is 1, 2, or a larger number for methods, respectively, for method categories 1, 2, and 3 above. RF echo signals are beamformed into spatial RF images using a range of n_s assumed tissue SoS values $\{s_1, \dots, s_{n_s}\}$. Image comparison metrics are calculated based on pairs of RF images, while image quality metrics are applied on B-Mode images (i.e., after envelope detection and log compression). The latter can be applied on a single B-mode image as well as on a compounded image from several frames. An overview for the image comparison (two frame) setting is illustrated in Figure 1.

A. Image Quality Metrics

Let $I \in \mathbb{R}^{n_x \times n_z}$ represent a beamformed ultrasound envelope image, where I is a matrix of pixel intensities on a grid of size $n_x \times n_z$ with lateral dimension x and axial dimension z . We study the following metrics.

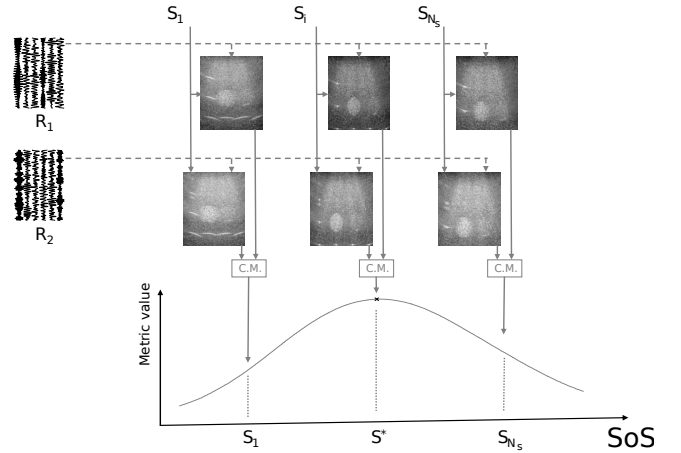


Fig. 1. Pipeline overview for optimizing a comparison metric (C.M.) between two acquisitions (R_1 and R_2) using trial-and-error of difference SoS values. Note that image quality and multi-frame statistic metrics work similarly, but instead with one or several acquisitions, respectively.

1) *Focus*: This metric is based on the observation [13] for natural images that certain frequency components in the Fourier domain are maximized when optimal image sharpness is achieved. We implement this for ultrasound imaging as the focus metric

$$\frac{\sum_{(f_x, f_z) \in F} |\text{FFT}(I)_{(f_x, f_z)}|^2}{\sum |\text{FFT}(I)|^2}, \quad (1)$$

where f_x and f_z are the spatial frequencies selected within a band F that contain frequency magnitudes between f_1 and f_2 , i.e., satisfying the criterion $f_1 \leq \sqrt{f_x^2 + f_z^2} \leq f_2$ which represents a ring in the Fourier domain.

2) *Entropy*: This leverages information theory principles to quantify image complexity based on the randomness of pixel intensity distribution, following the approach described in [14], with the metric defined on an intensity histogram as:

$$-\sum_{i=1}^{n_b} p(i) \log_2 p(i), \quad (2)$$

where $p(i)$ represents the probability of pixel intensities falling into histogram bin i , and n_b is the number of bins used for the histogram discretization. By assessing the distribution of pixel values, this metric evaluates the image's information content. High entropy suggests a potentially accurate SoS setting that uncovers details (more content) in $I(x, z)$, whereas low entropy indicates a less informative image.

3) *Gradient Magnitude (GradMag)*: This is based on the conventional understanding that a better focused (sharper) image would have larger gradient magnitudes, i.e.,

$$\sum_{x, z} G(x, z) = \sum_{x, z} \sqrt{g_x^2(x, z) + g_z^2(x, z)}, \quad (3)$$

where $g_x(x, z)$ and $g_z(x, z)$ are image gradients along the lateral and axial directions, respectively. The square root operation in (3) makes this metric less sensitive to few large gradients in the image.

4) *Tenengrad*: This is another gradient-based focusing metric proposed in [15], defined as:

$$\sum_{x,z} G^2(x,z) = \sum_{x,z} (g_x^2(x,z) + g_z^2(x,z)), \quad (4)$$

which emphasizes edge definition and structural details by considering squared gradient magnitudes, and is hence also more sensitive to large gradients compared to gradient magnitude metric above.

5) *ST-Ten*: We propose an adaptation of the Tenengrad metric for ultrasound imaging, which consists of three sequential steps designed to suppress US-characteristic noise and enhance sensitivity to SoS-related defocusing effects. The metric first start by smoothing the image by Gaussian filtering to reduce ultrasound-specific noise while preserving structural features.

$$I'(x,z) = \frac{1}{2\pi\sigma^2} e^{-(x^2+z^2)/(2\sigma^2)} * I(x,z) \quad (5)$$

Next, directional gradients are calculated as

$$g'_x = \partial I' / \partial x \quad g'_z = \partial I' / \partial z. \quad (6)$$

Then, our ST-Ten metric is computed as in Tenengrad but by only considering the magnitudes above a threshold τ as:

$$\sum_{x,z} G^2(x,z) = \sum_{x,z} (g_x'^2(x,z) + g_z'^2(x,z)), \quad \forall_{G(x,z) \geq \tau} \quad (7)$$

where the thresholding helps disregard many smaller gradients that would be less sensitive to defocusing from any incorrect SoS setting, which otherwise could overrun the total metric value. Such thresholding thus allows the metric to focus on structural edges that exhibit a clearer differentiation with SoS variation.

B. Image Similarity Metrics

These metrics are based on comparing two images, $I_1(x,z)$ and $I_2(x,z)$, each representing the same imaging field of view captured using differing acquisition sequences such that sound to an imaged point travels different acoustic paths from transmission to echo receive; e.g., plane waves with different transmission angles. When such acoustic paths differ, unless the correct SoS is utilized in beamforming for converting temporal signal to spatial images, the pixels of two images would not necessarily align. By leveraging this information, image-similarity metrics aim to identify the tissue SoS value as the one that minimizes discrepancy between beamformed images.

1) *Structural Similarity Index Metric (SSIM)*: This assesses image similarity based on a perceptual model considering texture, luminance, and contrast variations [16], defined as:

$$SSIM(I_1, I_2) = \left(\frac{2\mu_1\mu_2 + c_\mu}{\mu_1^2 + \mu_2^2 + c_\mu} \right) \cdot \left(\frac{2\sigma_{12} + c_\sigma}{\sigma_1^2 + \sigma_2^2 + c_\sigma} \right), \quad (8)$$

where μ_1 and μ_2 represent the average pixel intensities, σ_1^2 and σ_2^2 denote their variances, and σ_{12} is the covariance, within a small image patch that is scanned through the image as the metric is aggregated as a mean value between all patches. Constants c_μ and c_σ ensure stability for small denominators for the corresponding term. The metric produces values between -1 and 1 , where the latter indicates perfect structural similarity.

2) *Mean Squared Error (MSE)*: This metric quantifies pixel-wise differences between two images, defined as:

$$MSE(I_1, I_2) = \frac{1}{n_x n_z} \sum_{x=1}^{n_x} \sum_{z=1}^{n_z} (I_1(x,z) - I_2(x,z))^2. \quad (9)$$

This metric aims for direct intensity comparison. For consistency with the other introduced metrics, during SoS estimation we simply negate this metric, i.e., $-MSE$, such that the metric value is positively correlated with image similarity and is maximized at zero for images that are identical.

3) *Peak Signal-to-Noise Ratio (PSNR)*: This metric evaluates image similarity by quantifying the ratio between the maximum possible signal and the noise power [17], defined as:

$$PSNR(I_1, I_2) = 20 \cdot \log_{10} \left(\frac{\text{MAX}(I_1 \cup I_2)}{\sqrt{MSE}} \right), \quad (10)$$

where $\text{MAX}(I_1 \cup I_2)$ represents the maximum possible pixel value within both images. Note that the denominator is conventional root mean square error (RMSE), used here for assessing noise. PSNR metric is hence a normalized (and log-compressed) version of RMSE, where the normalization makes the metric dependent on input images and the square-root operator compared to MSE reduces sensitivity to few pixels with large differences (analogous to Gradient Magnitude vs. Tenengrad metrics for image gradient characterization).

4) *Mutual Information (MI)*: This metric measures statistical dependency between intensity distributions of two images, defined as:

$$MI(I_1, I_2) = \sum_i \sum_j p(i,j) \cdot \log \left(\frac{p(i,j)}{p(i)p(j)} \right), \quad (11)$$

where $p(i,j)$ represents the joint probability distribution of intensity values, and $p(i)$ and $p(j)$ are the marginal probability distribution functions of I_1 and I_2 intensities, respectively, computed from a 2D joint-intensity histogram of two images with n_b^2 bins. The metric thus reaches its maximum when intensity distributions exhibit strong statistical dependency, indicating optimal structural alignment between the images, without assuming linear or any algebraic relation between image intensity correspondences (hence allowing, e.g., cross-modality comparisons in other contexts).

5) *Correlation Coefficient*: This quantifies the linear relationship between pixel intensities, defined as:

$$\frac{\sum_{x,z} (I_1(x,z) - \bar{I}_1)(I_2(x,z) - \bar{I}_2)}{\sqrt{\sum_{x,z} (I_1(x,z) - \bar{I}_1)^2 \sum_{x,z} (I_2(x,z) - \bar{I}_2)^2}}, \quad (12)$$

where \bar{I}_1 and \bar{I}_2 denote the mean pixel values of respective images. The metric ranges between -1 and 1 , where the latter indicates perfect positive correlation suggesting optimal image alignment and hence a good beamforming SoS estimate.

C. Multi-Frame Statistics: Coefficient of Variation (CV)

This metric was proposed in [18] based on minimizing a normalized form of pixel variance between multiple frames, to evaluate the similarity between multiple frames collectively.

The metric is defined for a set $\{I_i\}$ of n_t images, i.e., $i \in \{1, 2, \dots, n_t\}$ as:

$$\text{CV}(\{I_i\}) = \sum_{x,z} \frac{\sigma_*(x,z)}{|\mu_*(x,z)|}, \quad (13)$$

where $\sigma_*(x,z)$ is the standard deviation and $|\mu_*(x,z)|$ is the mean of the absolute pixel magnitudes at an image location (x,z) across all the given n_t frames. This metric normalizes variance with average intensity to account for larger potential variances at higher magnitudes. Multiple frames are required to reliably calculate pixel-wise statistics.

III. RESULTS

A. Experimental Setup and Material

For evaluation we first utilize simulations with RF data obtained using k-Wave simulation software [19]. We generated three homogeneous tissue phantoms with known ground-truth speeds of sound $\hat{s} = \{1400, 1500, 1600\}$ m/s. We modeled the linear transducer used in the phantom experiments below, placed on a numerical domain of size 40×55 mm. Spatial and temporal simulation resolutions were set to be isotropic $75 \mu\text{m}$ and 6.25 ns, respectively. Tissue scatterers were simulated by slightly perturbing the medium density for a random 10% of the simulation grid pixels.

For evaluation on real data, we imaged two phantoms using a UF-760AG ultrasound system (Fukuda Denshi, Japan) and a linear transducer with 128 elements, $300 \mu\text{m}$ pitch, and 5 MHz center frequency. The first, Phantom1, is CIRS 040GSE (Norfolk, VA, USA) with a declared SoS of 1540 m/s. The second, Phantom2, is a custom CIRS SoS phantom, where the imaging was conducted in its homogeneous background region with a declared SoS of 1509 m/s. On each phantom, six different acquisitions were collected by mechanically fixing the probe on different locations.

A diverging wave Tx sequence was employed with a Tx aperture of 31 elements and a Virtual Source (VS) 9 mm behind the transducer surface, as in [20]. For all metrics, the entire imaging width of 38 mm and an axial field-of-view of 32 mm from $z = [8, 40]$ mm was considered to reduce the impact of near-field effects. In this imaging region, beamforming was performed for a grid of 256×3072 RF samples using Delay-and-Sum (DAS) algorithm using echo data received on all elements.

To assess image-quality metrics that require a single-frame, we used the B-mode images obtained with a single VS Tx centered on the transducer; with this sequence and data referred hereafter as *Single*. For image-comparison metrics, we used the beamformed RF data from two VS Tx events, separated 3.6 mm symmetrically around the center, called *Dual*. For assessing the multi-frame metric CV, we used the beamformed RF data from 17 Tx events, called hereafter *Full*. As the image-quality metrics can easily use arbitrary image input, we also tested this first group of methods on compounded images from the Dual and Full acquisitions.

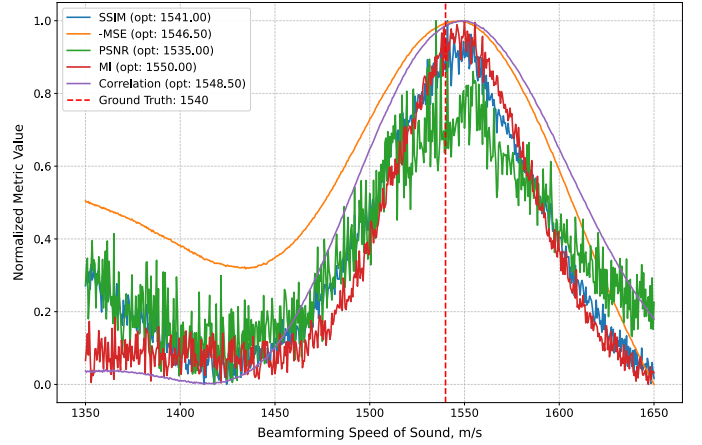


Fig. 2. Sample behavior of image comparison metrics, demonstrated for Phantom 1, by normalizing each metric between their minimum and maximum for visualization purposes. The optimum value (opt) found by each metric is indicated in the legend.

B. Implementation

The frequency bound parameters f_1 and f_2 of the Focus metric were set empirically based on grid search using the compounded Dual data from the simulation with $\hat{s} = 1500$ m/s. For gradient-based metrics (Gradient Magnitude, Tenengrad, ST-Ten), the Sobel operator with a kernel size of 3 was used to calculate spatial intensity gradients as proposed in [15]. The following metrics were implemented using standard libraries with default hyper-parameters: SSIM with `structural_similarity` and Entropy with `shannon_entropy` functions from the `scikit-image` python package, and Mutual Information with `mutual_info_score` from the `scikit-learn` python package by setting $n_b = 20$ bins.

For each Tx event, a series of images were beamformed across the n_s test SoS values in $s_i \in [1450, 1600]$ m/s with 0.5 m/s SoS increments. For this set of SoS values, having evaluated a metric $m(\cdot)$ using a set of one or more images $\{I_{n_t}\}$ depending on Single, Dual, or Full settings, an optimal global SoS value is then estimated by the given metric as $s^* = \arg \max_{s_i} m(\{I_{n_t}\}_{s_i})$. Sample patterns for the image comparison metrics are depicted in a normalized form in Figure 2.

C. Evaluation of Image-Based Global SoS Estimation

We evaluate the SoS estimation error by comparing to the known ground-truth of the corresponding experiment, i.e., the reported absolute error is $|s^* - \hat{s}|$. For simulations, mean absolute error (MAE) and standard deviation of the three homogeneous phantoms are reported. For the phantoms, the same statistics over the six data acquisitions are reported. The results for each metric are seen comparatively in Table I. Since the reported errors are bounded by the employed SoS search range, we highlight in red the average errors that are larger than 25% of the tested range, which then likely contain many estimations that are at the range bounds (e.g., , due to non-convex metric behaviour) and are hence vacuous. Although the image comparison and multi-frame statistic methods are

seen to perform similarly between different data domains, the image-quality metrics do not generalize well from Simulations to acquired Phantom data. Accordingly, the observations regarding image-quality metrics hereafter are given mainly based on the Phantom data.

The assessed image quality metrics are not successful when a single image is used. Notably, the error margin diminishes when images are compounded from multiple frames, rendering Focus and ST-Ten as viable options for SoS estimation. Comparison metrics overall show a markedly superior performance in all experiments when compared to image quality metrics. Notably, SSIM and MSE emerge as effective options for global SoS estimation in phantom data, with around 5 m/s accuracy. Regarding precision (measured via standard deviation of estimations), MSE and Correlation metrics are seen to perform well. Overall all given image-comparison metrics act as viable options for SoS estimation. The multi-frame statistic metric CV outperforms single-image quality metrics and performs on par with dual-frame image comparison metrics.

In Table I we also report the average metric computation time for a single beamforming SoS value, calculated in Python using the NumPy package on an Intel Core i7-12700K CPU with 64GB RAM. MSE is seen to be the fastest among all metrics, which makes it potentially the preferred metric of choice for global SoS estimation, given also its high accuracy, high precision, and relatively smooth metric behaviour as observed in Figure 2.

D. Sensitivity to Estimation Window Size

To further explore the potential use of image metrics for estimation based on small image regions of interest, we assessed them in subsequently smaller image patches. To that end, we halved the original 32 mm image depth consequently into smaller patches, i.e., $\{2, 4, 8, 16, 32\}$ equi-depth layers of each $\{16, 8, 4, 2, 1\}$ mm, respectively. Then, using the image in each such patch, the optimal SoS and the corresponding error is found as described earlier. For a more robust evaluation, we employed multiple (herein 4) estimations per patch, including the original 32 mm full image, by jittering its vertical location (layer depth) in increments of 0.4 mm. This analysis aims to assess the stability and consistency of the metrics, also with respect to processed image patch size. For this, we used the six acquisitions each from the two phantoms, while reporting the image quality metrics on the compounded Dual frame (given its superior performance from the earlier experiment). We report the results in Figure 3, separated for each metric and patch (layer) size, with data points indicating the error given a patch and its vertical jittered location.

Focus and ST-Ten are again observed as the only potentially viable image quality options, although the image comparison metrics largely outperform the image quality metrics. Among comparison metrics, Mutual Information and Correlation perform consistently and with overall high accuracy for all tested layer sizes down to 1 mm in our experimental setup. The performance of the multi-frame statistic metric CV is seen to deteriorate when the layer sizes are below 8 mm.

E. Global Optimality Assessment

We further study the cases when a metric may have a local optimum at the sought GT SoS value, but with a global optimum somewhere far from this value, e.g., at the bounds of the assessed SoS range. This is relevant for the cases where the original evaluation shows a large error value, which could have been reduced by considering a smaller SoS test range. For this, we performed an additional evaluation within a tighter SoS range of $s_i \in \{c_{GT} \pm 50\}$ m/s around each known ground-truth SoS value. The results are included in Table II and Figure 4. As seen in the figure, the metrics that have not performed satisfactorily in the earlier evaluation with a broad search range (e.g., Entropy, GradMag, Tenengrad overall; and MSE and PSNR for small layers) do not yield improved results when a smaller SoS search range is chosen either. The only appreciable improvement potentially is that the Single frame estimation becomes possible with under 20 m/s accuracy using ST-Ten metric, despite a relatively low precision.

IV. DISCUSSION

We have presented an extensive analysis of image-based metrics for model-free estimation of global SoS in simulations and phantoms. The metrics are categorized into image quality metrics that checks focusing quality by processing single (including compounded) B-mode images, image comparison metrics that measures the concordance between two frames, and multi-frame statistic metrics that evaluates the group-wise concordance via statistical techniques.

Summarizing our results while focusing on the phantom evaluations, none of the assessed image quality metrics performed satisfactorily when applied to a single image frame. Compounding two or more frames have improved their results, but still only the Focus and ST-Ten metrics attained some level of success. Comparatively, image comparison and statistic metrics have performed substantially superior across all the analyzed experimental scenarios. Notably, CV, MSE, MI, and Correlation emerged as effective metrics in analyzing large image patches including full frames. For smaller patch (layer) sizes, MI and Correlation yielded performance superior to all the other considered metrics, including CV and MSE. If a fast computation is desired, one can use MSE within relatively large image patches, i.e., regions of interest. If small patch sizes (layer resolutions) are desired, MI or Correlation are potential options. As the computation times are reported for full 32 mm image window, processing smaller patches would take shorter processing times.

Note that the image focusing or alignment at a point or in a patch deep inside the tissue is still dependent on all the superficial tissue regions that the acoustic waves need to travel through and that the beamforming time-delays should hence take into account. Accordingly, even when a metric is run in this paper locally in a patch or layer inside the tissue, the optimized SoS value is affected (in a weighted cumulative way) from all the shallower tissue regions that are encountered by the acoustic waves used in the beamforming of that patch. Therefore, if the involved sample is heterogeneous in SoS, then such effects need to be resolved, e.g., using

TABLE I

ABSOLUTE ERRORS (MEAN \pm STANDARD DEVIATION) OF GLOBAL SoS ESTIMATION USING DIFFERENT METRICS (ROWS) ARE REPORTED IN THREE DATASETS FOR USING SINGLE, DUAL, FULL (17 FRAMES) AS INPUT TO THE METHODS, WHERE APPLICABLE. IN SIMULATIONS, THE ERRORS ARE AVERAGE ACROSS RESULTS FROM THE THREE NUMERICAL PHANTOMS. FOR PHANTOMS, THE ERRORS ARE AVERAGE ACROSS SIX ACQUISITIONS EACH IN HOMOGENOUS BACKGROUND REGIONS WITH KNOWN DECLARED SoS VALUES. ERROR VALUES HIGHER THAN 75 m/s (25% OF SoS RANGE TESTED) ARE HIGHLIGHTED IN RED AS THEY POTENTIALLY CONTAIN SEVERAL SoS ESTIMATE AT RANGE BOUNDS AND ARE HENCE ONLY A LOWER-BOUND TO TRUE ABSOLUTE ERROR. FOR EACH EXPERIMENTAL SETTING (COLUMN), THE LOWEST ERROR (AND SIMILARLY THE STANDARD DEVIATION) IN EACH GROUP IS HIGHLIGHTED IN BOLD, WITH THE LOWEST ACROSS ALL THE GROUPS ALSO BEING UNDERLINED. PROCESSING TIME REQUIRED TO CALCULATE A METRIC AT A SINGLE BEAMFORMING SoS IS LISTED IN THE LAST COLUMN.

	Method	Simulations			Phantom 1			Phantom 2			Time [ms]
		Single	Dual	Full	Single	Dual	Full	Single	Dual	Full	
Quality	Focus	75.3 \pm 32.1	21.0 \pm 13.8	7.0 \pm 10.8	177.9 \pm 17.9	7.4 \pm 7.7	6.3 \pm 6.8	138.5 \pm 2.3	17.8 \pm 5.1	11.3 \pm 4.0	16
	Entropy	109.0 \pm 100.0	132.7 \pm 110.2	24.7 \pm 15.8	75.1 \pm 50.3	56.3 \pm 36.2	79.0 \pm 46.5	106.3 \pm 33.0	70.9 \pm 31.2	99.0 \pm 20.4	47
	GradMag	11.0 \pm 4.8	25.5 \pm 16.4	26.2 \pm 11.7	167.2 \pm 15.1	186.6 \pm 3.1	177.5 \pm 12.8	153.5 \pm 3.6	156.7 \pm 1.7	154.0 \pm 7.9	0.76
	Tenengrad	10.7 \pm 5.2	22.7 \pm 20.3	24.2 \pm 9.6	170.3 \pm 10.6	184.7 \pm 9.9	146.2 \pm 45.1	155.8 \pm 2.7	156.8 \pm 1.5	107.2 \pm 51.5	0.88
	ST-Ten	11.5 \pm 4.3	23.2 \pm 19.6	7.7 \pm 5.3	73.4 \pm 81.6	10.1 \pm 10.1	9.8 \pm 6.0	83.9 \pm 73.5	10.3 \pm 10.5	5.5 \pm 3.5	7.2
Comparison	SSIM	-	4.7 \pm 1.6	-	-	5.5 \pm 5.0	-	-	6.1 \pm 3.2	-	35
	MSE	-	13.2 \pm 1.9	-	-	6.1 \pm 0.7	-	-	4.6 \pm 1.4	-	0.34
	PSNR	-	9.2 \pm 6.2	-	-	7.2 \pm 5.6	-	-	7.7 \pm 7.3	-	0.45
	MI	-	6.8 \pm 4.0	-	-	6.8 \pm 2.3	-	-	7.2 \pm 3.3	-	37
	Correlation	-	1.8 \pm 1.4	-	-	8.8 \pm 1.4	-	-	7.3 \pm 1.4	-	6.6
	CV	-	-	4.8 \pm 1.5	-	-	4.5 \pm 0.4	-	-	5.4 \pm 0.7	62

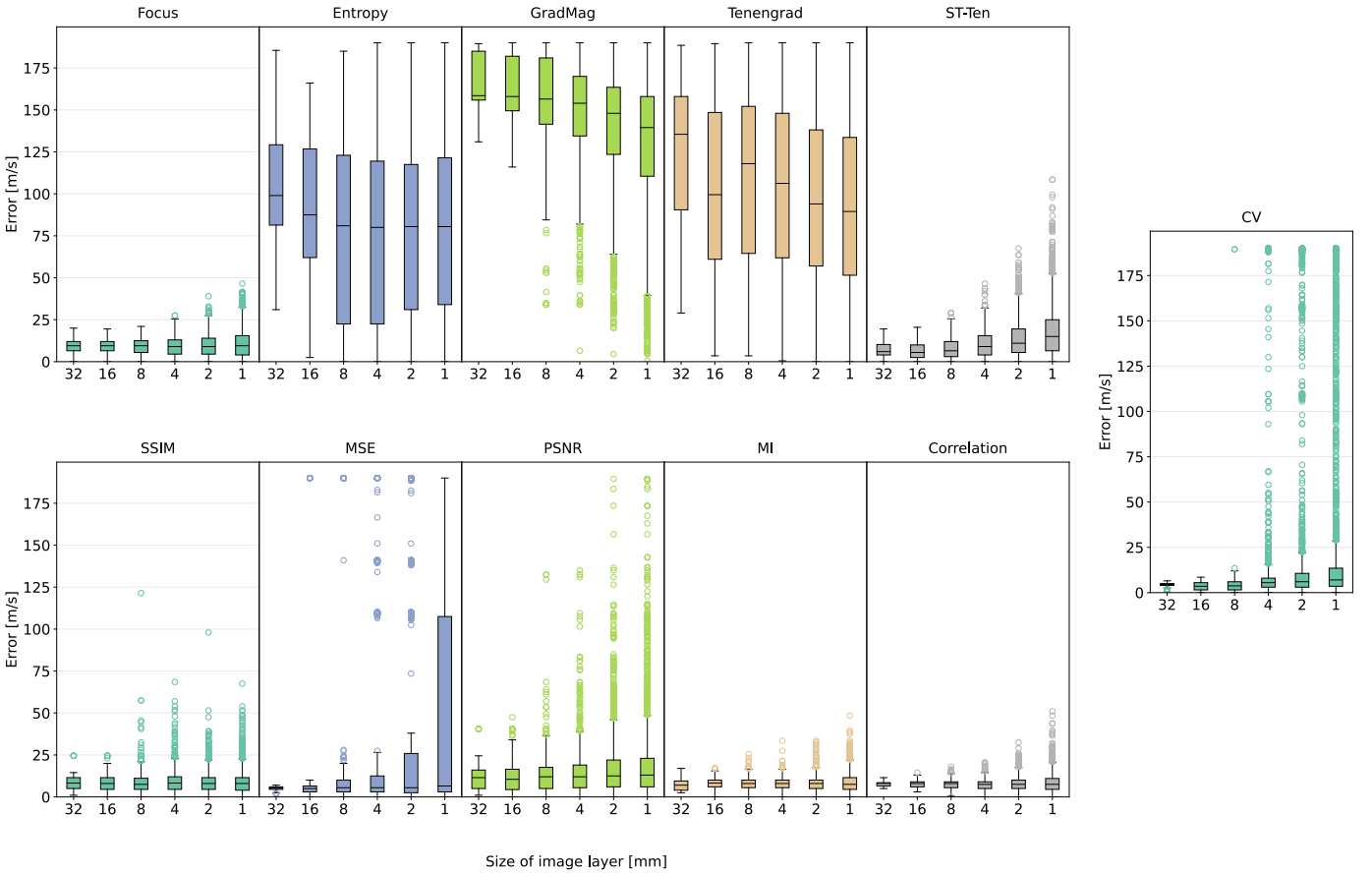


Fig. 3. To study the sensitivity of image-based metrics to utilized image window, the distribution of SoS estimation absolute errors are presented for using image patches (layers) of varying sizes from 32 down to 1 mm in depth. Each layer location is perturbed vertically in increments of 0.4 mm creating four layer positions each, in order to increase statistical stability of the evaluation. The evaluation is conducted for the two Phantoms using the Dual acquisition for the comparison and image-quality (via compounding) metrics, and using 17 VS Tx frames for CV. Accordingly, the distributions at 32 summarize 8 estimations (2 phantoms \times 1 32-mm-patch \times 4 perturbations), whereas at 1 summarize 256 estimations containing 32 1 mm-patches instead.

tomographic reconstruction [20] along acoustic paths involved in beamforming. Nevertheless, if the imaged sample is truly homogeneous, i.e., the SoS along any path is the same, then any patch-wise estimate including the entire frame would be equivalent in value, except for the signal-to-noise ratio of a metric reducing given smaller input data (patch pixels). That is the aspect we have evaluated in this work, where the study of image-based metrics in heterogeneous media and their layered or patch-wise SoS resolution was outside our current focus.

As in many estimation problems, repeatability (i.e., precision, represented herein by standard deviation) of measurements is arguably more important and relevant than absolute errors. This is first due to the fact that the actual SoS of samples in the experimental conditions may not be exactly as they are originally declared, due to the temperature differences or the phantoms drying over time. Furthermore, various assumptions in beamforming such as the Tx SoS setting and the fixed time offset (often referred as t_0) may shift the identified SoS value. Nevertheless, given highly repeatable measurements also sensitive to SoS variations, it is often possible to calibrate such absolute measurement errors with phantom samples of independently measured SoS. Furthermore, for differential evaluations, e.g., for diagnostic purposes, actual SoS values may be less relevant compared to their precise and repeatable differentiation capability, unless a standardization across multiple systems or setups are aimed in a future step. Note that MI and Correlation both provide relatively high precision, even in small image patches. Although CV demonstrates marginally higher precision for the entire frame, its repeatability rapidly reduces for smaller frames (even for half frame of size 16 mm) as observed in Figure 3, where the CV estimates (boxplot medians) seen to vary across different image sizes whereas Correlation preserves the median across images sizes; showing further promise for extending to a layered setting.

Image comparison and multi-frame statistic metrics can take arbitrary signals as input (pixel intensities), therefore we used post-beamformed RF data as a high-resolution input for them. Image image-quality metrics, on the other hand, mostly rely on the visual appearance based indicators, such as image gradients, so they cannot reliable function on RF signals given their modulated nature; therefore we used (envelope-detected) B-mode images as their input. Although these still contain characterized US speckle noise, it is seen from the results that some image-quality metrics, including Focus and our US-adapted ST-Ten, can still perform well to some extent in certain settings such as using compounded images. Their performance is indeed satisfactory for layered SoS estimation even for processing smaller image patches. These metrics hence become relevant when access to low-level RF data is not possible, as they operate on B-Mode images alone. Although a way to control the beamforming SoS (that the B-mode images are generated by) would still be necessary, such dynamic control is becoming more and more available in higher-end ultrasound systems, e.g., though a user-exposed knob, which can then also be controlled programmatically for testing on-the-fly multiple SoS values as studied in this paper.

V. CONCLUSIONS

We have studied different image-based metrics for estimating the medium SoS in simulation and phantom data. In particular, our two proposed metrics, ST-Ten and Focus, demonstrated remarkable performance among single-frame metrics, both in global and layered estimation scenarios. Image comparison metrics, particularly mean square error (MSE), mutual information (MI), and correlation metrics, demonstrated performance superior to image quality metrics. Multi-frame statistic metric Coefficient of Variation (CV) performed well for large image areas, but this approach requires multiple (many) frames, the acquisition and processing of which both incur larger times. This metric was also inferior to the above-mentioned image comparison metrics for processing smaller image patches. Image-based metrics have been shown to be an effective alternative to physical model-based approaches, minimizing reliance on model accuracy and robustness. Future research can explore these metrics in in-vivo conditions, extending them for resolving individual layer SoS values, or exploiting their potential in improving ultrasound image quality and diagnostic value.

REFERENCES

- [1] S. A. Goss, R. L. Johnston, and F. Dunn. Compilation of empirical ultrasonic properties of mammalian tissues. II. *The Journal of the Acoustical Society of America*, 68(1):93–108, 1980.
- [2] M. E. Anderson and G. E. Trahey. The direct estimation of sound speed using pulse-echo ultrasound. *The Journal of the Acoustical Society of America*, 104:3099–3106, 1998.
- [3] C. D. Bezek and O. Goksel. Analytical estimation of beamforming speed-of-sound using transmission geometry. *Ultrasonics*, 134, 2023.
- [4] D. Napolitano, C.-H. Chou, G. McLaughlin, T.-L. Ji, L. Mo, D. DeBusschere, and R. Steins. Sound speed correction in ultrasound imaging. *Ultrasonics*, 44:e43–e46, 2006.
- [5] H. C. Shin, R. Prager, H. Gomersall, N. Kingsbury, G. Treece, and A. Gee. Estimation of average speed of sound using deconvolution of medical ultrasound data. *Ultrasound in Medicine & Biology*, 36(4):623–636, 2010.
- [6] C. Yoon, Y. Lee, J. H. Chang, T. Song, and Y. Yoo. In vitro estimation of mean sound speed based on minimum average phase variance in medical ultrasound imaging. *Ultrasonics*, 51(7):795–802, 2011.
- [7] S. J. Park, J. Lee, W. Y. Lee, and Y. Yoo. Mean sound speed estimation with focusing quality evaluation for medical ultrasound imaging. In *2011 IEEE International Ultrasonics Symposium*, pages 2205–2208, 2011.
- [8] X. Qu, T. Azuma, J. T. Liang, and Y. Nakajima. Average sound speed estimation using speckle analysis of medical ultrasound data. *International Journal of Computer Assisted Radiology and Surgery*, 7(6):891–899, 2012.
- [9] H. Hasegawa and R. Nagaoka. Initial phantom study on estimation of speed of sound in medium using coherence among received echo signals. *Journal of Medical Ultrasonics*, 46:297–307, 2019.
- [10] C.-C. Shen and K.-L. Tu. Ultrasound DMAS beamforming for estimation of tissue speed of sound in multi-angle plane-wave imaging. *Applied Sciences*, 10(18):6298, 2020.
- [11] V. Perrot, M. Polichetti, F. Varray, and D. Garcia. So you think you can DAS? A viewpoint on delay-and-sum beamforming. *Ultrasonics*, 111:106309, 2021.
- [12] B. R. Chintada, R. Rau, and O. Goksel. Phase-aberration correction in shear-wave elastography imaging using local speed-of-sound adaptive beamforming. *Frontiers in Physics*, 9:690385, 2021.
- [13] K. De and V. Masilamani. Image sharpness measure for blurred images in frequency domain. *Procedia Engineering*, 64:149–158, 2013. International Conference on Design and Manufacturing (IConDM2013).
- [14] Amelia Carolina Sparavigna. Entropy in image analysis. *Entropy*, 21(5):502, 2019.
- [15] E. Krotkov. Focusing. *International Journal of Computer Vision*, 1(3):223–237, 1988.

TABLE II

LOCAL OPTIMALITY STUDY OF THE METRICS, BY RESTRICTING THE SoS SEARCH RANGE AROUND THE KNOWN SoS FOR EACH EXPERIMENT, I.E., $s_i \in \{c_{GT} \pm 50\}$ m/s. ABSOLUTE ERRORS (MEAN \pm STANDARD DEVIATION) OF GLOBAL SoS ESTIMATION USING DIFFERENT METRICS (ROWS) ARE REPORTED IN THREE DATASETS FOR USING SINGLE, DUAL, FULL (17 FRAMES) AS INPUT TO THE METHODS, WHERE APPLICABLE. IN SIMULATIONS, THE ERRORS ARE AVERAGE ACROSS RESULTS FROM THE THREE NUMERICAL PHANTOMS. FOR PHANTOMS, THE ERRORS ARE AVERAGE ACROSS SIX ACQUISITIONS EACH IN HOMOGENOUS BACKGROUND REGIONS WITH KNOWN DECLARED SoS VALUES. ERROR VALUES HIGHER THAN 25 m/s (25% OF SoS RANGE TESTED) ARE HIGHLIGHTED IN RED AS THEY POTENTIALLY CONTAIN SEVERAL SoS ESTIMATE AT RANGE BOUNDS AND ARE HENCE ONLY A LOWER-BOUND TO TRUE ABSOLUTE ERROR. FOR EACH EXPERIMENTAL SETTING (COLUMN), THE LOWEST ERROR (AND SIMILARLY THE STANDARD DEVIATION) IN EACH GROUP IS HIGHLIGHTED IN BOLD, WITH THE LOWEST ACROSS ALL THE GROUPS ALSO BEING UNDERLINED.

Method	Simulations			Phantom 1			Phantom 2		
	Single	Dual	Full	Single	Dual	Full	Single	Dual	Full
Quality									
Focus	50.0 \pm 0.0	21.0 \pm 13.8	7.0 \pm 10.8	46.6 \pm 2.8	7.4 \pm 7.7	6.3 \pm 6.8	39.6 \pm 8.9	17.8 \pm 5.1	11.3 \pm 4.0
Entropy	16.2 \pm 10.7	40.7 \pm 12.9	24.7 \pm 15.8	26.8 \pm 18.5	26.0 \pm 9.3	33.3 \pm 9.1	33.8 \pm 13.8	38.9 \pm 4.8	36.2 \pm 10.9
GradMag	11.0 \pm 4.8	25.5 \pm 16.4	26.2 \pm 11.7	40.8 \pm 13.0	27.1 \pm 16.7	49.4 \pm 1.2	41.0 \pm 6.6	25.0 \pm 14.3	47.8 \pm 4.1
Tenengrad	10.7 \pm 5.2	22.7 \pm 20.3	24.2 \pm 9.6	40.3 \pm 13.1	20.4 \pm 13.1	43.9 \pm 7.9	42.1 \pm 7.0	18.5 \pm 11.2	40.2 \pm 8.3
ST-Ten	11.5 \pm 4.3	23.2 \pm 19.6	7.7 \pm 5.3	19.0 \pm 15.1	10.1 \pm 10.1	9.8 \pm 6.0	19.5 \pm 20.6	10.3 \pm 10.5	5.5 \pm 3.5
Comparison									
SSIM	-	4.7 \pm 1.6	-	-	5.5 \pm 5.0	-	-	6.1 \pm 3.2	-
MSE	-	13.2 \pm 1.9	-	-	6.1 \pm 0.7	-	-	4.6 \pm 1.4	-
PSNR	-	9.2 \pm 6.2	-	-	7.2 \pm 5.6	-	-	7.7 \pm 7.3	-
MI	-	6.8 \pm 4.0	-	-	6.8 \pm 2.3	-	-	7.2 \pm 3.3	-
Correlation	-	1.8 \pm 1.4	-	-	8.8 \pm 1.4	-	-	7.3 \pm 1.4	-
CV	-	-	4.8 \pm 1.5	-	-	4.5 \pm 0.4	-	-	5.4 \pm 0.7

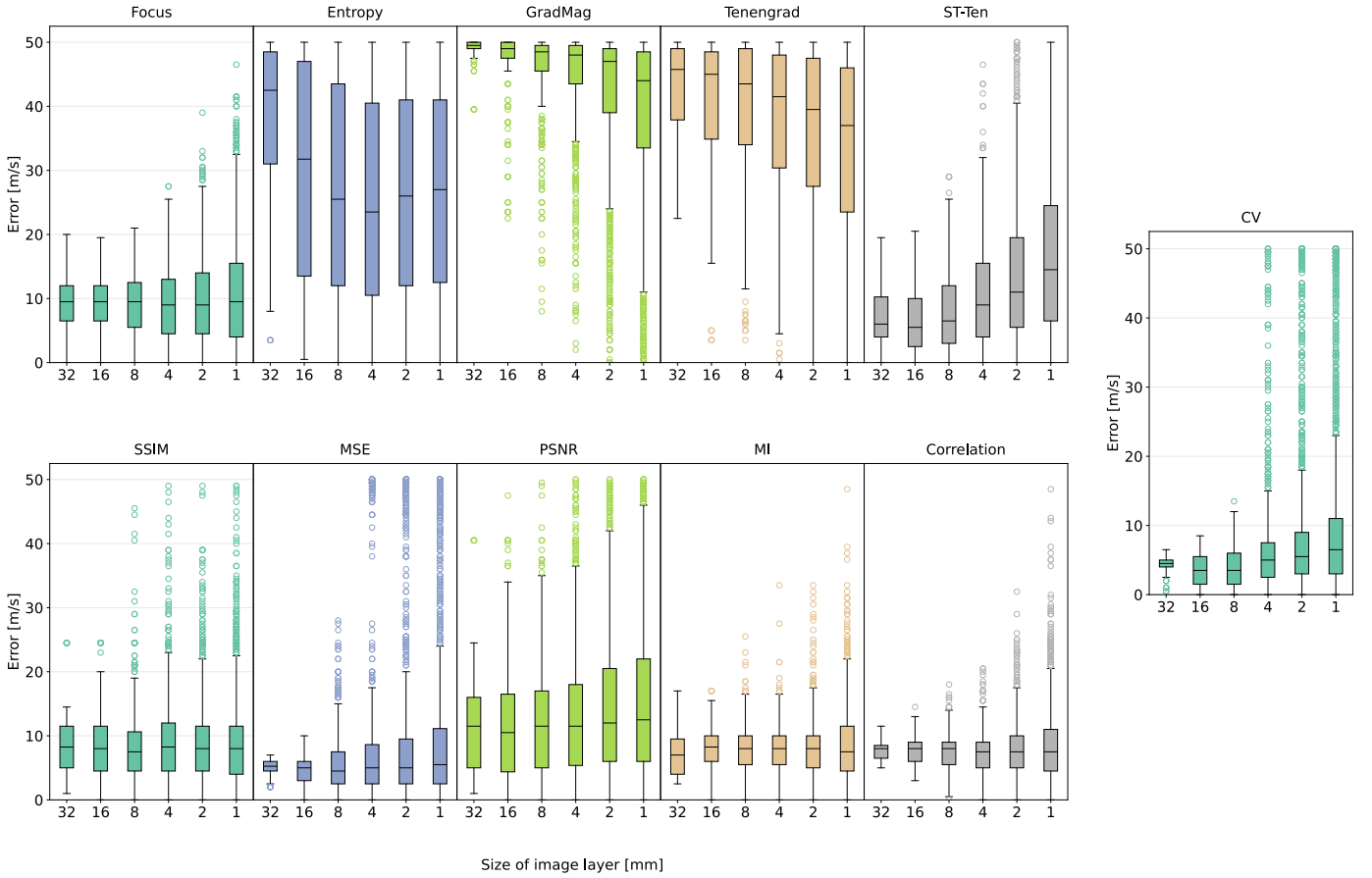


Fig. 4. The distribution of SoS estimation absolute errors are presented for using image patches (layers) of varying sizes from 32 down to 1 mm in depth, similarly to Figure 3 but when the SoS search range is restricted around the known SoS for each experiment, i.e., $s_i \in \{c_{GT} \pm 50\}$ m/s. Each layer location is perturbed vertically in increments of 0.4 mm creating four layer positions each, in order to increase statistical stability of the evaluation. The evaluation is conducted for the two Phantoms using the Dual acquisition for the comparison and image-quality (via compounding) metrics, and using 17 VS Tx frames for CV.

- [16] Z. Wang, A. C. Bovik, H. R. Sheikh, and E. P. Simoncelli. Image quality assessment: From error visibility to structural similarity. *IEEE Transactions on Image Processing*, 13(4):600–612, April 2004.
- [17] Q. Huynh-Thu and M. Ghanbari. Scope of validity of PSNR in image/video quality assessment. *Electronics Letters*, 44(13):800–801, 2008.
- [18] D. Xiao, P. De la Torre, and A. C. H. Yu. Real-time speed-of-sound estimation in vivo via steered plane wave ultrasound. *IEEE Transactions on Ultrasonics, Ferroelectrics, and Frequency Control*, 71(6):673–686, 2024.
- [19] B. E. Treeby and B. T. Cox. K-wave: MATLAB toolbox for the simulation and reconstruction of photoacoustic wave fields. *J. Biomed. Opt.*, 15(2):021314, 2010.
- [20] R. Rau, D. Schweizer, V. Vishnevskiy, and O. Goksel. Speed-of-sound imaging using diverging waves. *Int. J. Comput. Assist. Radiol. Surg.*, 16(7):1201–1211, Jul 2021.